RESEARCH ARTICLE

Influence of Processing Conditions on the Device Performance of PTB7: PCBM Based Organic Solar Cells: A Simulation Study

Ibad Ur Rahman[1], Kashif Ul Haq[1], Javid Ullah[1], Ibrar Ahmad[1,2,*], Mujahid Islam[1], Amin Ur Rehman[1], Khizar Hayat[1] and Said Karim Shah[1,3,*]

[1] Department of Physics, Abdul Wali Khan University Mardan, 23200 KP, Pakistan
[2] Department of Basic and Applied Sciences for Engineering, Sapienza University of Rome, Rome 00185, Italy
[3] Phyiscs Division, School of Science and Technology, University of Camerino, Camerino 62032, Italy

Abstract

This work reports the performance optimization of PTB7:PCBM-based inverted organic solar cells (IOSCs) using the Organic and Hybrid Materials Nano (OghmaNano) simulator. A comprehensive study was carried out by varying the key performance parameters, such as active layer thickness (AL), charge transport layers (CTLs), operating temperature, charge carrier mobilities(CCMs), and incident light intensity. The results showed that the carrier concentrations and mobilities (e.g, electron mobility (μ_e) and hole mobility (μh)) significantly changed with operating temperature (280 to 400 K), affecting the power conversion efficiency (PCE). Additionally, changing light intensity from 0.1 to 1.9 suns greatly impacted the short-circuit current density (Jsc) and open-circuit voltage (VOC). The addition of BPhen as the ETL and Spiro-OMeTAD as the HTL achieved an optimal device PCE of 16.12%. The overall finding demonstrated that these optimum device processing parameters are appropriate for the fabrication of inverted OSCs for industrial applications.

Keywords: inverted organic solar cells, drift diffusion model, donor/acceptor, charge transport layers, oghmaNano.

1 Introduction

The shift from non-renewable to renewable energy is required to meet the energy demands of the world while reducing the effects of climate change [1, 2]. Among the other non-renewable energy resources, fossil fuels have driven industrialization in the past, but they also pose serious environmental hazards in the form of greenhouse gas emissions and exhaustion of resources [3]. In contrast, renewable energy in the form of solar, wind, and hydroelectric energy

Submitted: 12 August 2025
Accepted: 02 November 2025
Published: 12 December 2025

Vol. 1, **No.** 1, 2025.
10.62762/JAEM.2025.834808

***Corresponding authors:**
✉ Ibrar Ahmad
Ibrar.ahmad@uniroma1.it
✉ Said Karim Shah
saidkarim@awkum.edu.pk

Citation
Rahman, I. U., Haq, K. U., Ullah, J., Ahmad, I., Islam, M., Rehman, A. U., Hayat, K. & Shah, S. K. (2025). Influence of Processing Conditions on the Device Performance of PTB7: PCBM Based Organic Solar Cells: A Simulation Study. *Journal of Advanced Electronic Materials*, 1(1), 24–38.

provides sustainable alternatives capable of meeting growing energy needs while also decreasing carbon footprints [4, 5]. In this regard, solar energy can be described as one of the most efficient alternative energy suppliers with many advantages that are endless, clean, quiet, and produce no pollution, making it highly relevant for large-scale solar cell production [6]. Solar cells use semiconductor material, whether organic or inorganic, which is the main part for solar energy conversion. Organic semiconducting material shows great promise owing to its flexible nature and tailor-made properties compared to inorganic semiconductors. Organic semiconductor-based flexible solar cells are gaining significant attention due to their numerous benefits, making them an auspicious material for renewable energy applications [7]. Conjugated polymer-based OSCs are promising substitutes for inorganic solar cells because of their low cost, lightness, flexibility, and room-temperature solution deposition on large-area substrates [8–10]. However, their low PCE limits large-scale commercialization. Efforts focus on improving OSC's efficiency with new materials and device engineering, and sophisticated designs [11]. Various simulation tools are used for solar cell modeling, such as SCAPS-1D [12–17] and OghmaNano, among others.

However, in this study, Oghma Nano is employed due to its user-friendly interface and high reliability. It provides comprehensive simulation models of organic, organic-inorganic hybrid solar cells [18–20]. Among various solar cell configurations, the OSCs in the inverted architecture were used to simulate high-efficiency solar cells due to their improved stability and flexible electron transport layer design [44]. Compared to direct OSC configurations, the inverted solar cell improves operational stability by replacing acidic and hygroscopic materials like PEDOT: PSS with more stable CTL. A breakthrough in inverted OSCs was achieved with the PTB7:PCBM system, which was among the first active layers to exceed 9% PCE in 2012, using a 5nm BPhen (ETL) [21]. Furthermore, optimization of inverted OSCs with solution-processed SnO_2 as the ETL and ternary blends such as PM6:PC_{71}BM:Y6 has led to outstanding performance enhancement, with an average PCE of 16.3%, with lower recombination and improved device stability under ambient conditions [22]. Recently, efforts have been made to enhance device performance and stability in inverted PTB7:PCBM-based OSCs using a solution-processed HTL. The stability was greatly enhanced with T80 lifetimes in excess of 2200 hours by minimizing burn-in losses and interfacial degradation [23]. Phenanthroline derivatives such as BPhen have been very promising in maximizing inverted OSC's efficiency by utilizing n-type doped BPhen (e.g., Cs_2CO_3:BPhen) facilitates better energy level alignment and enhanced conductivity, leading to enhanced PCEs from 1.34% to 4.1% in PTB7:PCBM devices, owing to enhancing electron extraction and morphology of the film [24]. The solution-casting BPhen onto Cs-halide layers in an attempt to improve device performance, reducing the recombination of charges and improving stability, resulting in PCE gains up to 46% and trivial degradation over weeks [25]. Likewise, the combination of CdS with diphenyl-substituted phenanthroline molecules such as BPhen and BCP enhanced interfacial contact and electron mobility, boosting device efficiency from 3.09% to 8.36% in PTB7:P_{71}BM device [26]. Recently, doping ZnO with Cs2CO3:BPhen lowered surface defect-related degradation and enhanced the PCE of PM6:Y6 inverted devices from 15.54% to 17.09% and remained at 83% efficiency after 1000 hours without encapsulation, proving its dual functionality in enhancing performance and stability [27]. Besides, because of its physical and electrical properties, Spiro-OMeTAD, as the first solid-state HTL developed for perovskite solar cells, has been a conventional material. 4-tBP and LiTFSI are commonly used even though they adversely affect the long-term device lifetime, particularly through their hygroscopicity and corrosiveness. Its efficiency is directly related to the type and dopant concentration [28]. Building on this, the research work aims to combine PTB7: PC70BM as AL, BPhen as ETL, and Spiro-OMeTAD as HTL into an IOSC device configuration would enhance PCE and device stability even further. By optimizing interfacial energy alignment and charge transport, this study seeks to reveal new avenues for low-cost, high-performance IOSCs in industrial production [29].

2 Device Modeling and Simulations

2.1 Simulation Methodology

We employ the OghmaNano simulator for comprehensive electrical modeling, which is a tool for the simulation of optoelectronic devices [20, 30, 31], such as OLEDs and OFETS, especially thin-film solar cells [32, 33]. OghmaNano provides correct results as it solves the drift-diffusion and Poisson equations with the chosen statistics [34–36]. One of the main limitations of this simulation software

is that it assumes ideal, uniform layers, ignoring real-world material heterogeneity such as non-uniform defects, grain boundaries, and degradation. However experimentally, materials have grain boundaries, different types of non-uniform defects, and chemical reactions at interfaces.

In this study, we employ a 1-D mathematical model to solve the complete set of semiconductor equations, namely the electron and hole continuity and drift-diffusion equations coupled with Poisson's equation, together with appropriate carrier statistics [37]. The solver also includes detailed physical models (e.g., multi-trap Shockley Read-Hall recombination [38], band-to-band/Langevin recombination [39], etc.) and supports both Maxwell-Boltzmann and Fermi-Dirac carrier statistics, making it well-suited to disordered materials such as organic or perovskite semiconductors [40, 41]. It allows all device parameters (for example, band gaps, mobilities, trap densities, doping, etc.) to vary with position in the stack, enabling the modeling of graded layers and AL thicknesses. The temperature can be changed to perform temperature-dependent simulations. The fundamental equations used in this model are as follows [42, 43]:

$$\frac{d}{dx}\epsilon_0\epsilon_r\frac{d\phi}{dx} = q(n-p) \tag{1}$$

$$\frac{\partial J_n}{\partial x} = q\left(R_n - G + \frac{\partial n}{\partial t}\right) \tag{2}$$

$$\frac{\partial J_p}{\partial x} = -q\left(R_p - G + \frac{\partial p}{\partial t}\right) \tag{3}$$

$$J = J_n + J_p \tag{4}$$

$$J_n = q\mu_n n\frac{\partial E_c}{\partial x} + qD_n\frac{\partial n}{\partial x} \tag{5}$$

$$J_p = q\mu_p p\frac{\partial E_v}{\partial x} - qD_p\frac{\partial p}{\partial x} \tag{6}$$

Where q is the elementary charge, ϵ_0 is the permittivity of vacuum, ϵ_r is the relative permittivity of an organic semiconductor material, and the variable ϕ is the electrostatic potential, and x is the position in a direction normal to a device surface. J, J_n and J_p are the total, electron, and hole current densities. Similarly, R_p, R_n are the rates of recombination of electrons and holes, G is the photogeneration rate, D_p, D_n represent the diffusion coefficient of holes and electrons, and μ_p and μ_n are the mobilities of the free electrons and holes of the active layer.

The carrier concentrations within the device were calculated using Maxwell–Boltzmann approximations for non-degenerate semiconductors. For this method, electron and hole concentrations are expressed by the following relations:

$$n = N_c \exp\left(\frac{F_n - E_c}{K_B T}\right) \tag{7}$$

$$p = N_v \exp\left(\frac{E_v - F_p}{K_B T}\right) \tag{8}$$

In these equations, F_n and F_p are the quasi-Fermi energy levels for electrons and holes, respectively. E_c and E_v are the conduction and valence band energies, while N_c and N_v are the effective density of states in the corresponding bands. K_B is Boltzmann's constant, and T is the absolute temperature. These equations are fundamental in semiconductor device modeling, enabling the exact computation of carrier distributions under both thermal equilibrium and non-equilibrium conditions.

The simulation process was done step by step to enhance the device performance. Various device structures were initially made by considering appropriate boundary conditions and material parameters. The optimum CTL was selected by optimizing ETL and HTL. For uniformity of later experiments, the AL was then optimized to 170 nm. Besides, the impact of temperature on the device capacitance and CCM was studied. Impedance simulation was used to study charge transport dynamics and recombination processes. The optimized structure generally improved PCE substantially, with useful information for the development of high-performance OSCs.

2.2 Device Design and Energy Band Alignment of IOSC

The optimal structure of IOSC (see Figure 1(a)) employs Spiro-OMeTAD as the HTL and BPhen as the ETL, while Figure 1(b) shows the working principles of the IOSCs, where the light absorption in the AL forms excitons, which are split to free charge carriers. The electrons are transported toward the cathode by means of the ETL, and the holes are transported toward the anode by means of the

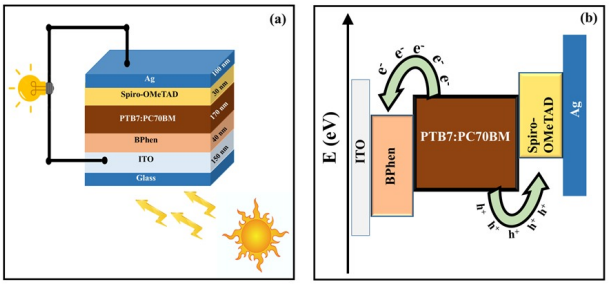

Figure 1. (a) Structural diagram, and (b) energy level diagram showing charge transport routes.

HTL. Better energy level alignment facilitates efficient transportation, resulting in efficient charge separation and suppressing recombination losses, which is critical for achieving high performance.

The impact of different ETLs and HTLs on the performance of IOSCs was systematically analyzed. Various ETLs such as PEDOT:PSS, Spiro-OMeTAD, PMMA, P3HT, CuO, BCP, and NT4N, and HTLs such as TPBI, TiO_2, ZnO, SnO_2, C_{60}, and BPhen were used to enhance the key performance parameters like PCE, FF, V_{oc}, and J_{sc}. The optimized device consists of Spiro-OMeTAD as the ETL and BPhen as the HTL, giving maximum PCE while the thickness of the PTB7/PCBM was maintained at 110 nm. The optimal device structure (see Figure 2) consisted of Ag/Spiro-OMeTAD/PTB7:PC70BM/BPhen/ITO. BPhen was shown to be an efficient HTL through its better energy level alignment with the AL, enabling efficient hole extraction and transport. Its high hole mobility helps in minimizing the charge recombination, thereby enhancing device performance.

BPhen's transport properties of charge and reduced energy losses are better than other HTLs such as TPBI, TiO_2, ZnO, SnO_2, and C_{60}. Similarly, Spiro-OMeTAD is set aside from the rest of the ETLs as it possesses higher hole conductivity and efficient charge transport characteristics, both of which help with improved carrier collection and less interfacial resistance. Although there are other alternatives, such as PEDOT:PSS and PMMA, Spiro-OMeTAD is the ideal option for improved efficiency due to fewer limitations on stability and hole transport.

2.3 Simulation Settings and Parameters

Simulation settings and the AL parameters were all taken from the literature [45–47]. Basic active layer parameters were all considered carefully, including optical bandgap, effective density of the states, relative permittivity, carrier mobilities, trap densities, and tail slope. Table 1 lists the important values utilized in the simulation. To facilitate precise device modeling, refractive index and absorption information were also obtained from some published articles [48, 49]. It was revealed from the prior works that the bandgap of PTB7:PC70BM ranges from 1.0 and 2.1 eV and depends on the reason, such as the method of measurement and the structure of the film. In the current work, a band gap value of 1.59 eV was chosen from the literature [37, 50, 51].

Table 1. Summarized parameters used for simulation.

Parameters	SI Units	Numerical Values
Electron mobility	$m^2\ V^{-1}\ s^{-1}$	2.48×10^{-7} [52]
Hole mobility	$m^2\ V^{-1}\ s^{-1}$	2.48×10^{-7} [52]
Effective density of free electron states	m^{-3}	1.28×10^{27} [52]
Effective density of free hole states	m^{-3}	2.86×10^{25} [52]
Electron trap density	$m^{-3}\ eV^{-1}$	3.8×10^{26} [52]
Hole trap density	$m^{-3}\ eV^{-1}$	1.45×10^{25} [52]
Electron tail slope	eV	0.04 [52]
Hole tail slope	eV	0.06 [52]
Free electron to trapped electron	m^{-2}	2.5×10^{-20} [52]
Trapped electron to free hole	m^{-2}	1.32×10^{-22} [52]
Trapped hole to free electron	m^{-2}	4.67×10^{-26} [52]
Free hole to trapped hole	m^{-2}	4.86×10^{22} [52]
Number of traps bands	—	20 [52]
Relative permittivity	au	3.9 [53]
Xi	eV	3.75 [54]
Eg	eV	1.59 [55, 56]

3 Results and Discussions

The creation of excitons as a result of photon flux to the donor/acceptor interface and the subsequent splitting of excitons into holes and electrons to produce electricity are explained in detail in the following sections. PTB7:PCBM blend with different electron and hole transport layers of varying thicknesses was employed to study the performance of the OSCs, simulated by OghmaNano, which includes comprehensive details of device operational parameters based on optoelectronic characteristics of OSCs.

In real-world thin-film OSCs, performance is often affected by factors such as energetic disorder, trap-assisted recombination, and variants in film

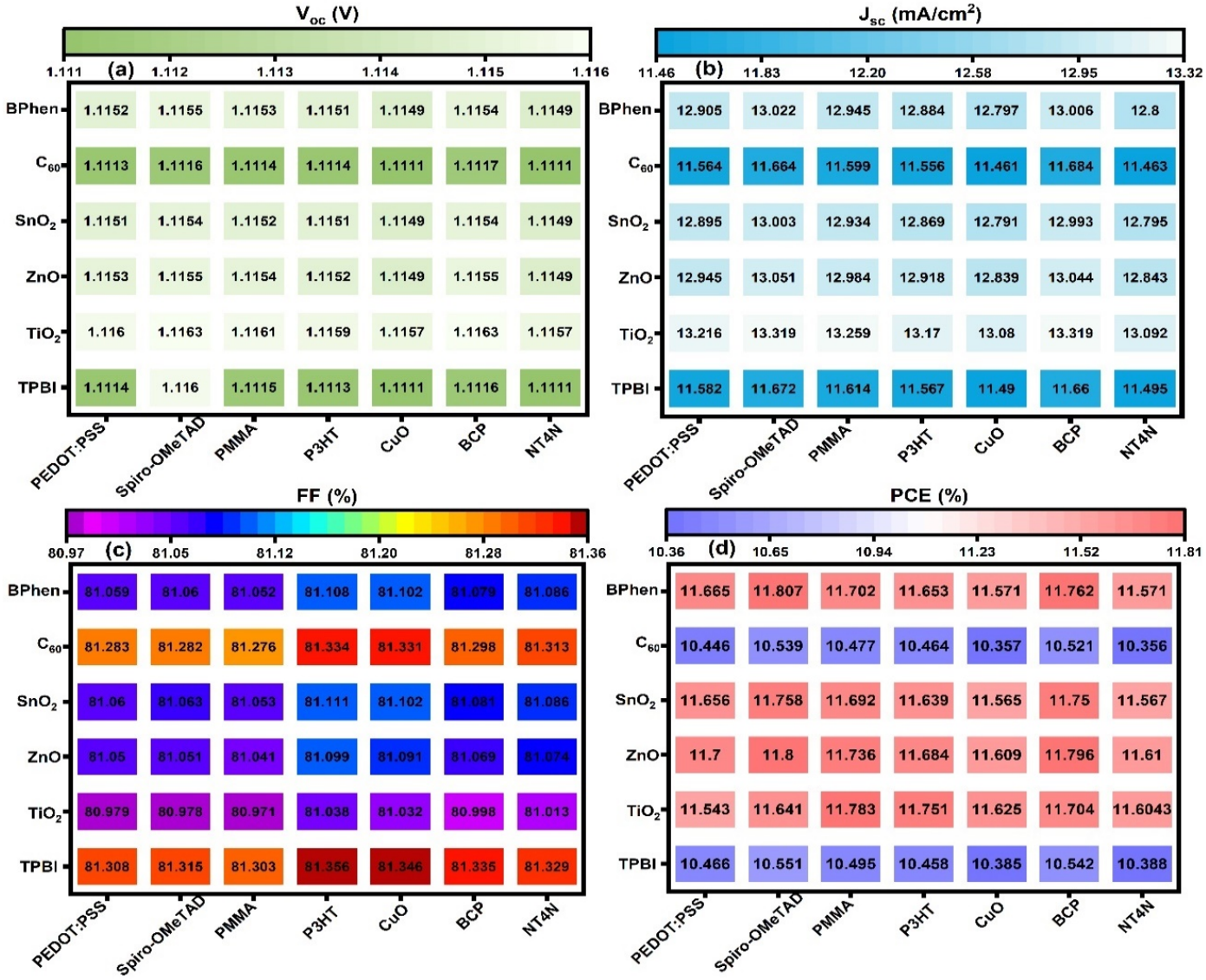

Figure 2. Impact of different ETL/HTL materials on V_{oc}, J_{sc}, PCE, and FF.

homogeneity, which are not entirely signified in ideal simulation models. To reduce this gap, our calculation for the PTB7:PC70BM-based inverted architecture utilized realistic physical parameters, including defect density, trap densities, and carrier mobilities, to make the device more realistic. The electron trap density ($3.8 \times 10^{26}\,\mathrm{m^{-3}\,eV^{-1}}$) and $1.45 \times 10^{25}\,\mathrm{m^{-3}\,eV^{-1}}$ for holes and tail slopes (0.04–0.06 eV) are added to represent defect-related recombination, whereas charge carrier mobility ($2.48 \times 10^{-7}\,\mathrm{m^2\,V^{-1}\,s^{-1}}$) represents scattering effects introduced by morphological irregularities and structural. All these parameters together characterize the effect of interfacial defects, grain boundaries, and phase inhomogeneity on recombination processes and carrier transport. This method helps to establish a dependable and realistic framework for investigating and enhancing the performance of PTB7:PC70BM-based OSCs.

3.1 Thickness Optimization of PTB7:PCBM

Optimizing the PTB7:PCBM thickness is crucial for enhancing the efficiency of solar cells. A thicker layer harvests more light but increases the rate of recombination; too thin reduces absorption. Simulations between 110 and 290 nm indicated that J_{sc} increases with thickness up to 290 nm due to improved incoming radiation absorption, which generates more photo-generated excitons [57], then worsens likely due to defects. FF declines with thickness increase due to series resistance [58]. At optimum AL thickness of 170 nm, the PCE reached 16.034% with an FF of

74.214 %, J_{sc} 19.4 mA/cm^2, and V_{oc} of 1.12 V. J–V curves shown in Figure 3(b). At lower thickness absorb less light, whereas at higher thickness (e.g., 290 nm) face higher recombination. V_{oc} remains stable but may drop slightly to high thickness. Balancing absorption, recombination, and charge extraction at 170 nm yields the highest efficiency, highlighting the optimal thickness.

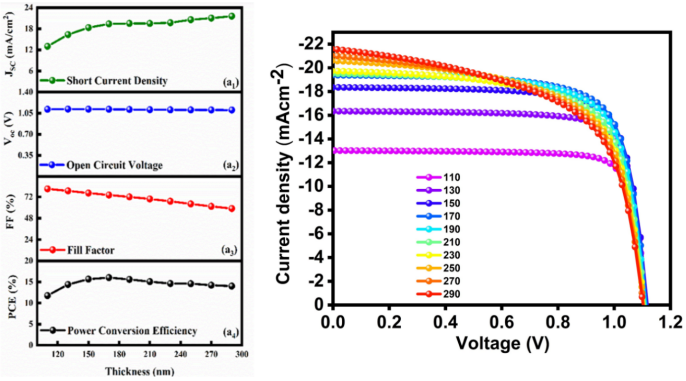

Figure 3. (a) Effects of active layer thickness on efficiency, Voc, Jsc, and FF, (b) J-V response for various thickness conditions.

3.2 Effect of Working Temperature on Device Performance

The primary photovoltaic properties of IOSCs were assessed with varying temperatures from 280 K to 400 K to observe the thermal effect on the device efficiency. At 330 K, V_{oc} decreases with rising temperature due to increased recombination and reduced V_{oc} (1.0843 V) [59], J_{sc} remains stable with slight gains at higher temperatures, reaching 19.398 mA/cm^2. PCE first rises to 16.120%, then falls since recombination prevails at 330 K, and the FF remains close to 76.642%, showing maximum charge extraction. This indicates that 330 K provides the optimal balance between charge generation and recombination. Figure 4(b) illustrates that with an increase in temperature, V_{OC} falls due to more recombination, while J_{sc} remains unchanged, indicating temperature primarily influences V_{OC} and FF, which causes the device performance to vary.

3.3 Effect of Temperature on the Device Capacitance

The capacitance and other performance characteristics of inverted OSCs are significantly influenced by various temperatures. The capacitance in Figure 5(a) is comparatively high at 280 K, reaches its maximum at 300 K, then slowly reduces while the temperature increases to 320 K, 340 K, and so on. This trend can be understood based on how temperature acts on charge carriers. The capacitance is large at 280 K due to charge

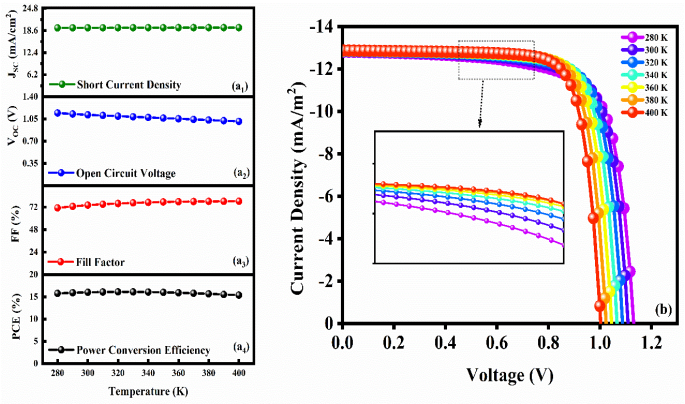

Figure 4. (a) Effect of operating temperature on device parameters, (b) J-V characteristics at different temperatures.

carriers, but the width of the depletion is still decent. When the temperature is increased to 300 K, thermal excitation also generates more free carriers, decreasing the depletion width and creating a total capacitance larger [60]. At temperatures above 300 K, capacitance decreases, probably due to more recombination of thermally generated carriers before they can contribute to charge build-up. Also, higher temperatures result in more intense lattice vibrations, lowering carrier mobility [61] and subsequently reducing capacitance. In Mott–Schottky analysis, the $1/C^2$ vs. voltage is plotted in Figure 5(b). At higher temperatures, the slope of $1/C^2$ decreases, indicating a reduction in the built-in potential (V_{bi}) and depletion width. The higher slope shows a more noticeable depletion effect at lower temperatures, for example, 280 K and 300 K, with more localized charge carriers and a larger potential barrier [62]. This transition means that the electrical properties of the IOSC are affected by band alignment and distribution changes taking place at high temperatures.

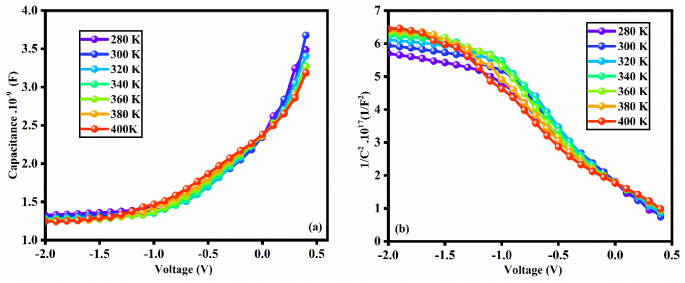

Figure 5. (a) Capacitance-voltage measurements at various temperatures, and (b) Mott-Schottky plot (1/C² vs. V) at various temperatures.

3.4 Temperature Effect on Charge Carrier Transport

In OSCs, for instance, PTB7:PCBM blends, charge transport is controlled mainly by thermally activated hopping from localized molecular sites. As one proceeds to higher temperatures, carriers acquire enough thermal energy to overcome trap states and energetic disorder, leading to enhanced mobility [63]. The graphs show how temperature and open circuit voltage affect CCM in an OSC (see Figure 6), illustrating various conditions like electron, hole, average mobilities at maximum power, J_{sc}, and V_{oc}. Electron mobility at maximum power increases with temperature and voltage, indicating fewer scattering effects and better charge transport. A similar trend is observed for hole mobility, which rises due to enhanced hopping transport typical for organic semiconductors. The average mobility at maximum power, combining both carriers, also increases with temperature, facilitated by thermal activation overcoming trap sites. The mobility at short-circuit current density increases with temperature, though minor variations occur from recombination and electric fields. Conversely, average mobility at open-circuit voltage shows decreasing or undefined values, likely due to charge recombination or extraction issues at higher temperatures. Increased temperature enhances mobility by enabling charge carriers to overcome traps through thermal energy, improving molecular ordering, but excessive thermal disorder can saturate or reduce mobility [64].

3.5 Effect of sunlight intensity

The quantity of sunlight intensity is an important factor to consider when describing the performance and efficiency of photovoltaic systems since it affects the formation of charge carriers within the solar cell, and thus the overall electrical output [65]. Figure 7(b) illustrates the J–V curves of IOSCs at varying suns ranging from 0.3 to 1.9 sun. The best performance was observed at an optimum sun intensity of 1 sun, resulting an efficiency of 16.12%. It is observed that the J_{sc} increases with the increasing the sun intensity while the V_{oc} slightly varies, demonstrating efficient charge separation and collection at the respective electrodes. The curves at Figure 7(a) show how IOSCs photovoltaic properties change with light intensity from 0.3 to 1.9 sun. The increasing trends in the device performance parameters with higher sun intensity demonstrates the significant effect of irradiation of OSCs. The V_{OC} slightly varies with increasing sun intensity which is mainly depend on the photoactive layer's built-in potential and recombination losses. The J_{sc} increases linearly with sun intensity which is the most important factor contributing to the enhanced output under irradiation the OSCs. Moreover, there is slight loss observed in the FF with increasing the sun intensity, which might be attributed the effect higher recombination or series resistance. The PCE of 16.12% was achieved at the optimum sun intensity (1 sun), with other optimum device performance parameters such as a FF of 76.64 %, V_{OC} 1.08 V and a J_{sc} of 19.398 mA/cm^2. The loss of PCE at higher sun intensity is due to resistive and recombination losses.

3.6 The Intensity-Dependent Behavior of IOSC: Probing Performance and Loss Mechanisms

The performance of IOSC as a function of different light intensities reveals its working and loss mechanisms. Figure 8(a) shows voltage increases logarithmically with intensity, as more photogenerated charge carriers lead to splitting of more quasi-Fermi levels, bringing the voltage closer to its maximum. This phenomenon is due to the diode equation, as $V_{oc} \propto \left(\frac{kT}{q}\right) \ln(I)$ [66]. The J_{sc} is rising linearly, following a typical power law ($J_{sc} \propto I^{\alpha}$, with $\alpha < 1$). The non-ideal behavior arises mainly due to the accumulation of space charge caused by unbalanced mobility of electrons and holes, preventing current extraction with higher intensity [59, 67]. The recombination time constant in Figure 8(b) reduces as illumination increases, since greater carrier density enhances recombination, shortening lifetimes. In the meantime, effective carrier mobility slightly increases with intensity. This trend is related to trap filling, in which increased carrier densities fill up shallow traps to allow freer transport and to morphology effects that enhance percolation paths [68]. The initially extracted charge shown in Figure 8(c) rises with light intensity. However, at high illumination levels, the rise becomes sublinear, which indicates a balance between improved carrier generation and greater recombination losses. At extremely high intensities the balance tilts in favor of bimolecular recombination, and the steady-state carrier concentration follows a linear dependence on the square root of generation rate ($n \propto G^{1/2}$). If charge is normalized with intensity and carrier lifetime reverses the trend: the extracted charge drops quickly before saturating, as in Figure 8(d). This suggests the loss of collection efficiency at high generation rates, when extraction is overwhelmed by recombination. This regime clearly demonstrates recombination-limited behavior, wherein efficiency of extraction reduces with bimolecular recombination channels taking control.

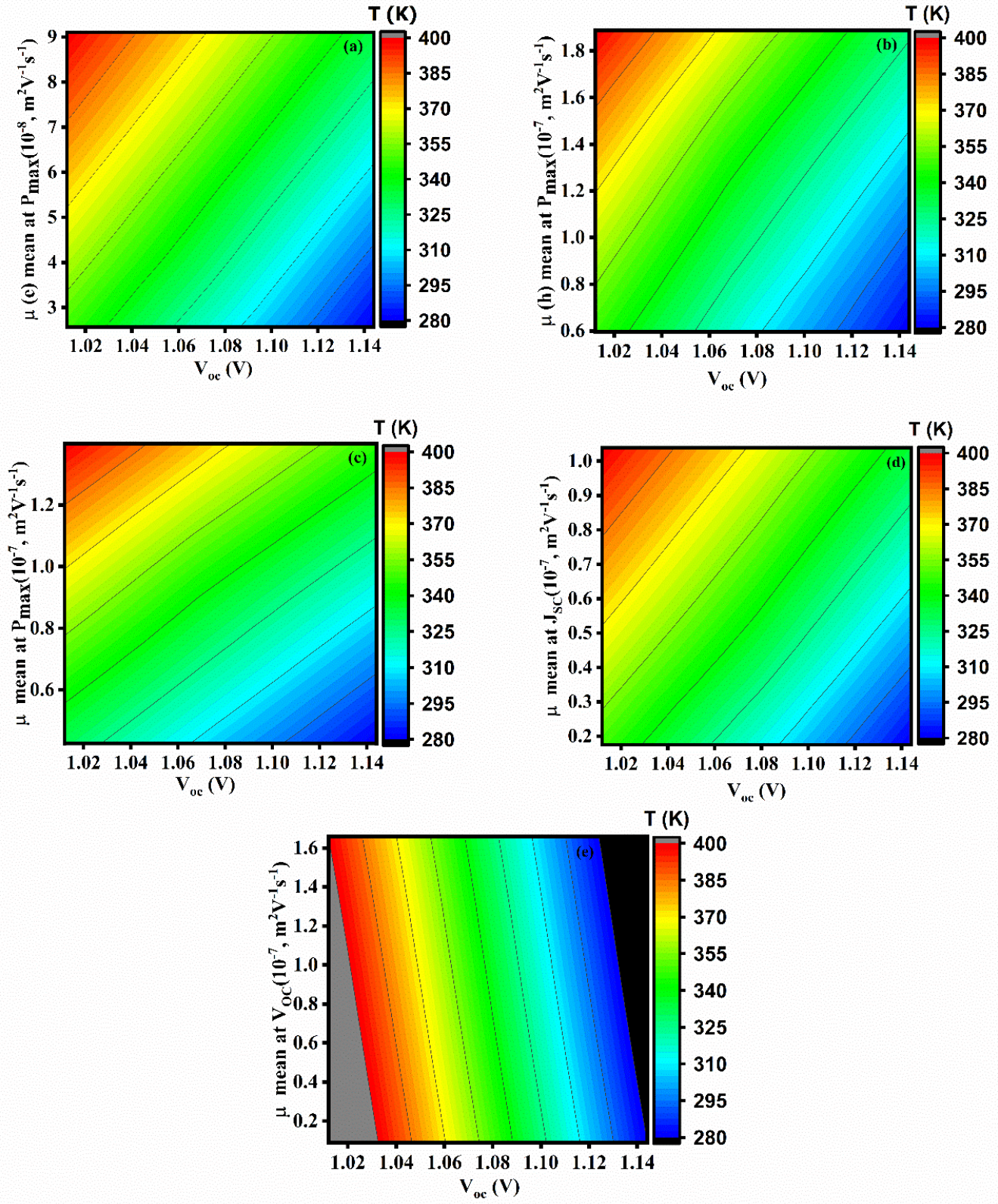

Figure 6. Temperature-dependent plots of carrier mobility: (a) Electron mobility at Pmax, (b) Hole mobility at Pmax, (c) Average mobility at Pmax, (d) Average mobility at Voc, (e) Average mobility at Jsc.

Light intensity characterization reveals recombination mechanisms and transport limitations and constitutes a valuable diagnostic for device optimization.

3.7 Charge Transport and Recombination Study Using Impedance Spectroscopy

Impedance spectroscopy (IS) studies in organic solar cells under various light intensities and voltages

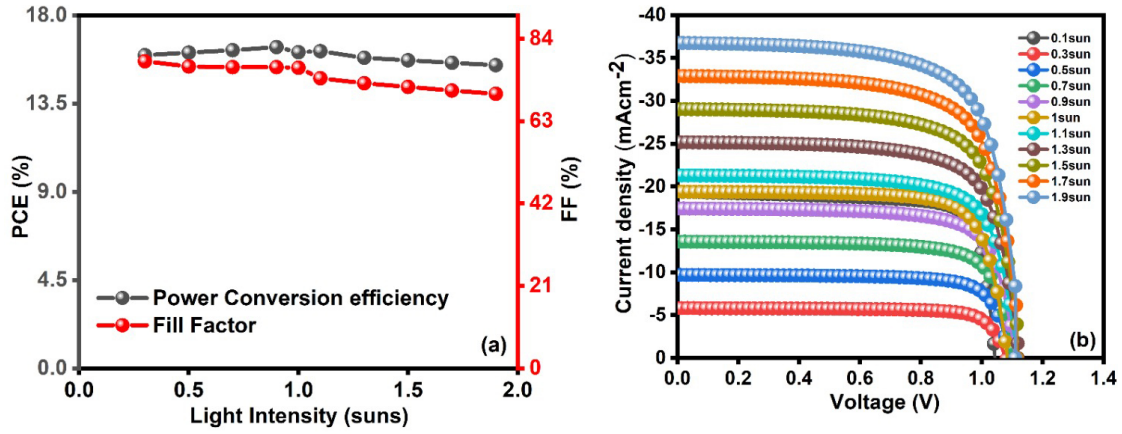

Figure 7. (a) The impact of sunlight intensity on device parameters, (b) characteristics under different sunlight intensities.

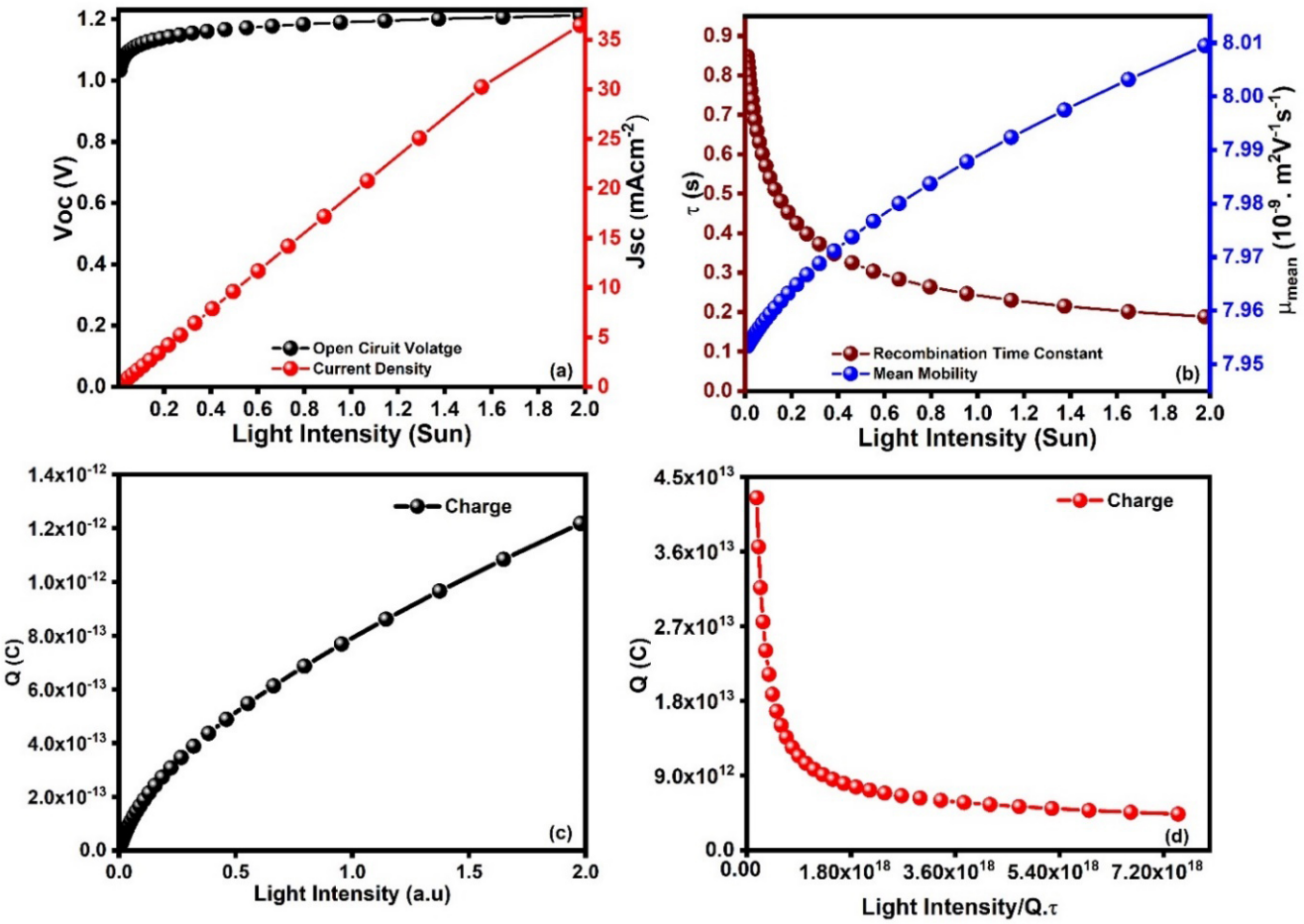

Figure 8. Light intensity dependence of important organic solar cell parameters: (a) V_{oc} and J_{sc}, (b) recombination lifetime (τ) and mobility (μ), (c) extracted charge, and (d) charge versus normalized intensity.

examine the influence of light and applied voltage on charge recombination and transport. Figure 9(a) shows that the semicircle in the Nyquist plot decreases as the sun intensity increases, resulting decrease in charge transport resistance [69, 70]. At lower intensities (0.1 or 0.3 sun), the impedance is higher due to fewer charge carriers and increased resistive losses. The maximum efficiency of 16.12% was achieved at 1 sun when recombination and charge generation are equal. Figure 9(b) illustrates impedance at different voltages. When an external voltage is applied, carrier transport improves. High recombination resistance is indicated by impedance peaking at 0V, which decreases as the voltage reaches 0.7 V, suggesting better charge injection and reduced losses. Figure 9 illustrates how sunlight intensity and applied voltage influence

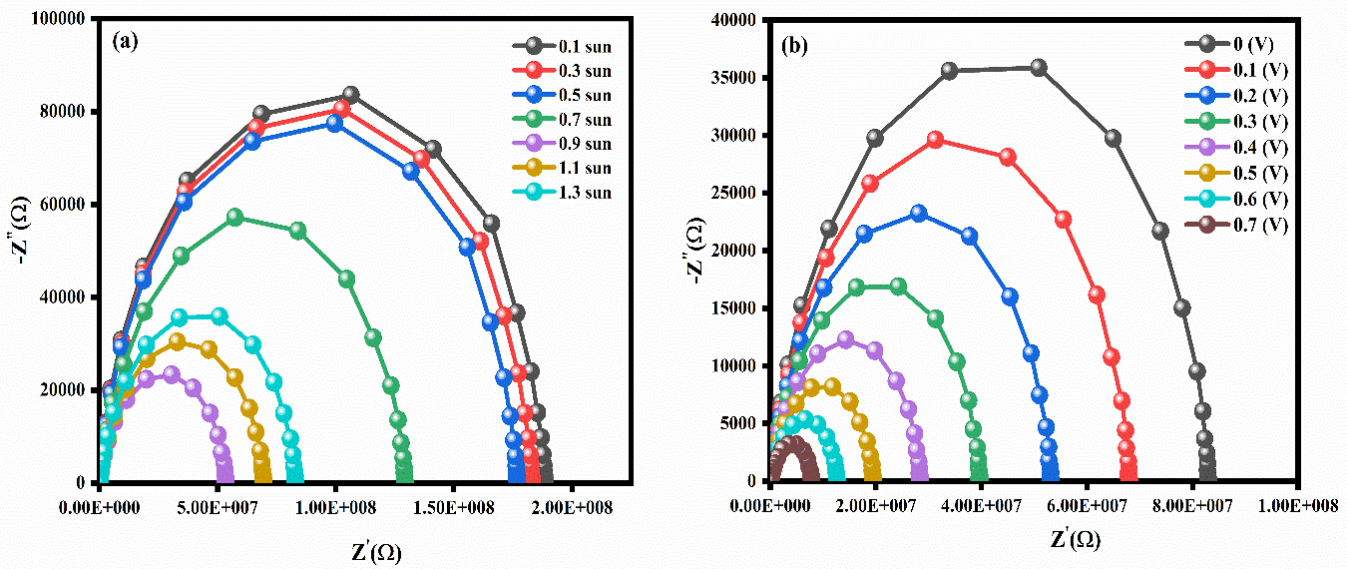

Figure 9. (a) Impedance spectra under varying illumination intensities, (b) impedance response at different applied voltages.

Table 2. Theoretical and experimental analysis of electrical parameters in PTB7:PC70BM-based OSCs.

Device Configuration	FF (%)	J_{sc} (mA/cm^2)	V_{oc} (V)	PCE (%)	Data Type	Ref.
ITO/PEDOT:PSS/PTB7:PC70BM/AL	65.3	13.14	0.60	5.20	Simulated	[37]
ITO/PEDOT:PSS/PTB7:PC70BM/AL	75.6	15.27	0.60	6.98	Simulated	[71]
ITO/PEDOT:PSS/PTB7:PC70BM/EFN-Br/Ag	68.05	16.34	0.73	8	Simulated	[53]
ITO/ZnO/PTB7:PC70BM/MoO_3/Ag	56.9	13.74	0.75	5.87	Experimental	[72]
ITO/ZnO/PTB7:PC70BM/MoO_3/Ag	69	14.93	0.70	7.2	Experimental	[73]
Glass/ITO/ZnO/PTB7:PC70BM/MoO_3/Ag	69.97	13.5	0.73	6.95	Experimental	[74]
ITO/ZnO/ PFEOSO$_3$Na/PTB7	69	16.63	0.74	8.49	Experimental	[75]
ITO/ZnO:Au NPs/PTB7Th:PC71BM/MoO_3/Ag	67.8	22.3	0.79	11.8	Experimental	[76]
ITO/ZnO/PEOz nanodots/PTB7Th:PC71BM/MoO_3/Ag	71.2	19.0	0.794	10.74	Experimental	[77]
Ag/Spiro-OMeTAD/PTB7:PC70BM/BPhen/ITO	76.64	19.398	1.08	16.12	This study	—

efficiency, with an optimum sun intensity of 1 sun.

3.8 Comparative analysis of the OSCs

Figure 10(a) shows the J–V characteristics of the optimum device operational parameters. Compared to the initial device efficiency, the enhanced device performance was obtained by utilizing the optimized AL thickness (170 nm), ETLs, sun intensity (1 sun), and working temperature (330 K). The maximum PCE of 16.12% was obtained with optimized device operational parameters. The optimized device exhibited the other performance parameters such as V_{oc} of 1.08 V, J_{sc} = 19.398 mA cm^{-2}, and an FF of 76.64%. In addition, the OSC configuration was modified as Ag/Bphen/PTB7:PCBM/Spiro-OMeTAD/ITO, by replacing the ETL and HTL positions, referred to as conventional OSC. The J–V curves for optimal conventional OSC were measured. The high efficiency of 15.77% was obtained from the optimal conventional OSC along with the other performance parameters such as V_{oc} of 1.081 V, J_{sc} of 17.03 mA cm^{-2}, and FF of 77.15%. Figure 10(b) illustrates the comparative analysis of both OSCs. The results demonstrate that the PCE of the inverted OSC is higher than that of the conventional OSC. It might be attributed to the better energy level alignment of the materials, resulting in better charge carrier extraction and transport to the respective electrodes in the case of inverted OSCs as compared to the conventional counterpart.

To accurately evaluate the simulation model, it should be compared with data from recent experiments on PTB7:PCBM-based OSCs. As shown in Table 2, this comparison outlines simulated device parameters with experimental results. The outcome shows that the simulation aligns with the common performance trends observed in experiments with V_{OC}, J_{sc}, FF, and PCE. Moreover, the improved device configurations suggested here have superior performance parameters and achieve a maximum efficiency of 16.12% (V_{oc} = 1.08 V, J_{sc} = 19.398 mA/cm^2, FF = 76.64%). These

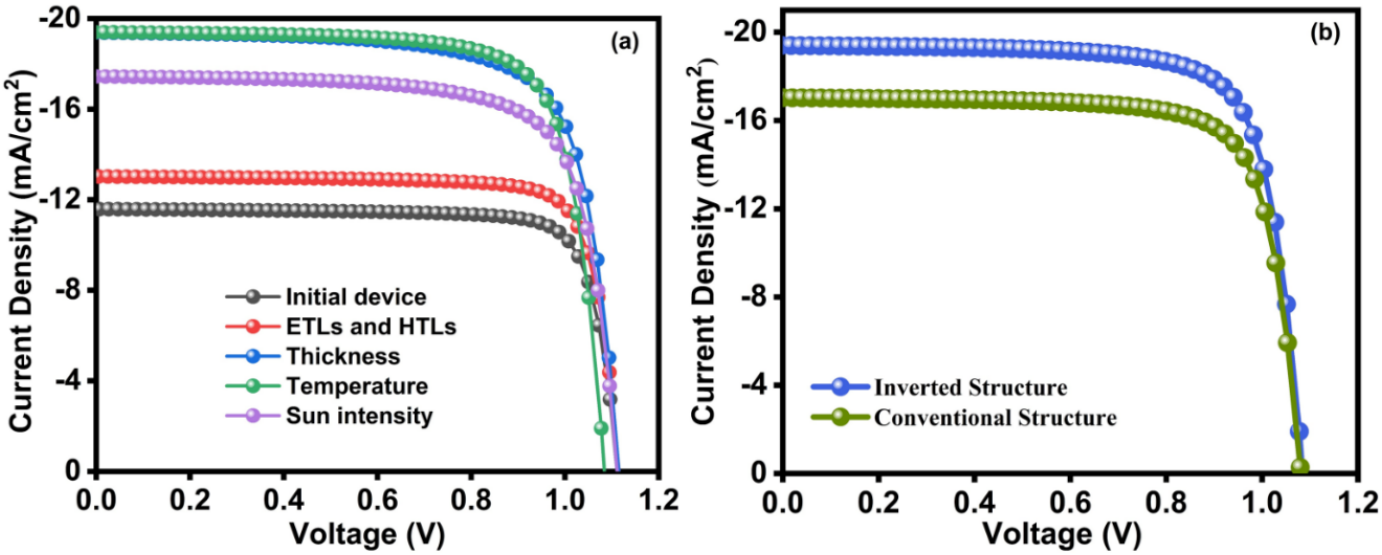

Figure 10. (a) J–V characteristics of initial and optimized devices under optimized ETLs, active layer thicknesses, temperatures, and light intensities, (b) J–V curves of conventional and inverted OSCs.

values exceed the model's predictions and previous experimental results achieved, thereby serving as confirmation of the applicability of the model to reliable estimation of performance and designing high-efficiency devices. Future experiments will be marked by the precise fabrication and characterization of these improved structures under real-world conditions. This research will help to validate the simulation, improve the understanding of charge transport and interface interaction, and eventually bridge the theoretical modeling–practical device implementation gap.

4 Conclusion

In this research work, we have systematically investigated the performance parameters of inverted PTB7:PCBM OSC and the impact of different hole and electron transport materials, operating temperatures, light intensity, and impedance behaviors. The higher performance IOSC was obtained by using BPhen as ETL and Spiro-OMeTAD as HTL. Under optimal device parameters, i.e., the AL thickness of 170 nm, operating temperature of 330 K, light intensity of 1 sun, and charge carrier mobility of $2.48 \times 10^{-7}\,\mathrm{m^2V^{-1}s^{-1}}$, the device achieved the maximum PCE of 16.12%, FF of 76.64%, V_{oc} of 1.08 V, and a J_{sc} of 19.398 $\mathrm{mA/cm^2}$. The findings verify the advantages of inverted organic architecture over standard OSC, with enhanced charge carrier generation, better carrier transport behavior, and efficient carrier collection to corresponding electrodes. The findings provide an enabling platform for rational design and fabrication of high-efficiency IOSCs and open up new avenues for the prospective realization of future next-generation organic photovoltaics for large-scale commercial production.

Data Availability Statement

Data will be made available on request.

Funding

This work was supported by the Higher Education Department of Khyber Pakhtunkhwa under Project ID 3118 (No. PMU/1-22/HEREF/2014-15/Vol-VIII/7294).

Conflicts of Interest

The authors declare no conflicts of interest.

Ethical Approval and Consent to Participate

Not applicable.

References

[1] Suman, A. (2021). Role of renewable energy technologies in climate change adaptation and mitigation: A brief review from Nepal. *Renewable and Sustainable Energy Reviews, 151*, 111524. [CrossRef]

[2] Shamoushaki, M., & Koh, S. L. (2024). Solar cells combined with geothermal or wind power systems reduces climate and environmental impact. *Communications Earth & Environment, 5*(1), 572. [CrossRef]

[3] Ang, T. Z., Salem, M., Kamarol, M., Das, H. S., Nazari, M. A., & Prabaharan, N. (2022). A comprehensive study of renewable energy sources: Classifications,

challenges and suggestions. *Energy strategy reviews, 43*, 100939. [CrossRef]

[4] Kaushik, B., Chandel, P., & Saini, M. (2024). Renewable energy technology. In *Sustainability in Digital Transformation Era: Driving Innovative & Growth* (pp. 413-420). CRC Press.

[5] Belman-Flores, J. M., Camacho-Vázquez, G., & Rodríguez-Muñoz, A. P. (2016). A review of hybrid systems including photovoltaic solar energy: General aspects in Mexico. *Journal of Renewable and Sustainable Energy, 8*(4). [CrossRef]

[6] Lee, H. Y., & Huang, H. L. (2014). Performance improvement of pentacene-doped P3HT: PCBM inverted polymer solar cells with AZO nanorod array passivated using photoelectrochemical technique. *Organic Electronics, 15*(7), 1362-1367. [CrossRef]

[7] Wang, T., Chen, M., Sun, R., & Min, J. (2023). Recent research progress of all-polymer solar cells based on PSMA-type polymer acceptors. *Chem, 9*(7), 1702–1767. [CrossRef]

[8] Abdallaoui, M., Sengouga, N., Chala, A., Meftah, A., & Meftah, A. (2020). Comparative study of conventional and inverted P3HT: PCBM organic solar cell. *Optical Materials, 105*, 109916. [CrossRef]

[9] Pelzer, K. M., & Darling, S. B. (2016). Charge generation in organic photovoltaics: a review of theory and computation. *Molecular Systems Design & Engineering, 1*(1), 10-24. [CrossRef]

[10] Imamura, S., Mizutani, T., Kojima, K., & Ochiai, S. (2011). Characteristics and performance of organic photovoltaic cells having the active layer fabricated by ternary organic semiconducting materials. *Journal of Photonics for Energy, 1*(1), 011119-011119. [CrossRef]

[11] Maoz, M., Abbas, Z., Shah, S. A. B., & Lughi, V. (2025). Recent advances in flexible solar cells; materials, fabrication, and commercialization. *Sustainability, 17*(5), 1820. [CrossRef]

[12] Bibi, K., Ahmad, I., Hayat, K., Ali, M., & Shah, S. K. (2022). Simulation and experimental device performance analysis of TiO2-based inverted organic solar cells. *Journal of Electronic Materials, 51*(9), 5181–5187. [CrossRef]

[13] Ahmad, I., Hayat, K., Ashraf, M., Imran, M., & Shah, S. K. (2023). SCAPS-based simulation analysis of device parameters of ZnO-inverted polymer solar cells. *Optical and Quantum Electronics, 55*(4), 345. [CrossRef]

[14] Ahmad, I., Hayat, K., Ashraf, M., Imran, M., & Shah, S. K. (2023). ZnO-based inverted organic solar cells: a comparative analysis of simulation and experimental devices. *Physica Scripta, 98*(11), 115962. [CrossRef]

[15] Mushtaq, S., Tahir, S., Ashfaq, A., Bonilla, R. S., Haneef, M., Saeed, R., ... & Amin, N. (2023). Performance optimization of lead-free MASnBr3 based perovskite solar cells by SCAPS-1D device simulation. *Solar Energy, 249*, 401-413. [CrossRef]

[16] Alahmadi, A. N. (2025). Numerical analysis and design of hole and electron transport layers in lead-free MASnIBr2 perovskite solar cells. *Eng, 6*(9), 222. [CrossRef]

[17] Osman, B. A., Shaker, A., Ahmed, I. S., & Abdolkader, T. M. (2025). Unveiling the role of dual grading in device optimization of HTL-free Sb2 (S, Se) 3 solar cells. *Scientific Reports, 15*(1), 27050. [CrossRef]

[18] Çiloğlu, P., Tretmans, C., Deibel, C., Pietschmann, J. F., Stoll, M., & MacKenzie, R. C. (2025). Visualizing the Link Between Nanomorphology and Energetic Disorder in 3D Organic Solar Cells. *arXiv preprint arXiv:2507.20040*.

[19] Zhu, L., Zhang, M., Xu, J., Li, C., Yan, J., Zhou, G., … & Hou, J. (2022). Single-junction organic solar cells with over 19% efficiency enabled by a refined double-fibril network morphology. *Nature Materials, 21*(6), 656–663. [CrossRef]

[20] Ahmad, I., Hayat, K., Ashraf, M., Imran, M., & Shah, S. K. (2025). Experimental and computational insights into optimizing polymer solar cell operational parameters. Current Applied Physics. [CrossRef]

[21] He, Z., Zhong, C., Huang, X., Wong, W.-Y., Wu, H., Chen, L., … & Cao, Y. (2012). Enhanced power-conversion efficiency in polymer solar cells using an inverted device structure. Nature Photonics, 6(9), 591–595. [CrossRef]

[22] Liu, Z., Wang, L., Zhao, H., Chen, P., & Xie, X. (2023). High-performance inverted ternary organic solar cells using solution-processed tin oxide as the electron transport layer. Organic Electronics, 120, 106828. [CrossRef]

[23] Sung, Y. M., Tsao, C. S., Lin, H. K., Cha, H. C., Jiang, P. C., Liu, T. C., ... & Tsay, J. S. (2023). Dramatic improvement in the stability and mechanism of high-performance inverted polymer solar cells featuring a solution-processed buffer layer. *Nanoscale, 15*(7), 3375-3386. [CrossRef]

[24] Xu, Z. Q., Yang, J. P., Sun, F. Z., Lee, S. T., Li, Y. Q., & Tang, J. X. (2012). Efficient inverted polymer solar cells incorporating doped organic electron transporting layer. *Organic Electronics, 13*(4), 697-704. [CrossRef]

[25] Xiao, T., Fungura, F., Cai, M., Anderegg, J. W., Shinar, J., & Shinar, R. (2013). Improved efficiency and stability of inverted polymer solar cells with a solution-processed BPhen interlayer and polystyrene beads. *Organic Electronics, 14*(10), 2555-2563. [CrossRef]

[26] Liu, X., Li, X., Li, Y., Wang, X., & Wang, Z. (2016). CdS–phenanthroline derivative hybrid cathode interlayers for high performance inverted organic solar cells. *Journal of Materials Chemistry A, 4*(3), 297–302. [CrossRef]

[27] Park, S., Kim, J., Lee, H., & Park, S. (2025). Interface engineering with BPhen: Cs2CO3 for high-performance and stable inverted nonfullerene

organic solar cells. *Solar RRL, 9*(3), 2400902. [CrossRef]

[28] Nakka, L., Cheng, Y., Aberle, A. G., & Lin, F. (2022). Analytical review of spiro-OMeTAD hole transport materials: paths toward stable and efficient perovskite solar cells. *Advanced Energy and Sustainability Research, 3*(8), 2200045. [CrossRef]

[29] Luo, W., Li, Y., Zhang, J., & Wang, Z. (2019). Dopant-free Spiro-OMeTAD as hole transporting layer for stable and efficient perovskite solar cells. *Organic Electronics, 74*, 7–12. [CrossRef]

[30] Erray, M., Hanine, M., Boufounas, E.-M., & El Amrani, A. (2018). Combined effects of carriers charge mobility and electrodes work function on the performances of polymer/fullerene P3HT: PCBM based organic photovoltaic solar cell. *The European Physical Journal Applied Physics, 82*(3), 30201. [CrossRef]

[31] Singh, N., Chaudhary, A., Saxena, S., Saxena, M., & Rastogi, N. (2017). Electrical simulation of organic solar cell at different charge carrier mobility. *IOSR Journal of Applied Physics, 9*(2), 1-4. [CrossRef]

[32] Salgado-Conrado, L., Álvarez-Macías, C., & Reyes-Durán, B. (2024). A review of simulation tools for thin-film solar cells. Materials, 17(22), 5213. [CrossRef]

[33] Boudia, M. E. A., Wang, Q., & Zhao, C. (2024). Optimization of the active layer thickness for inverted ternary organic solar cells achieves 20% efficiency with simulation. *Sustainability, 16*(15), 6159. [CrossRef]

[34] MacKenzie, R. C. I., Balderrama, V. S., Schmeisser, S., Stoof, R., Greedy, S., Pallarès, J., ... & Von Hauff, E. (2016). Loss mechanisms in high efficiency polymer solar cells. *Advanced Energy Materials, 6*(4), 1501742. [CrossRef]

[35] Gao, Y., MacKenzie, R. C., Liu, Y., Xu, B., van Loosdrecht, P. H., & Tian, W. (2015). Engineering Ultra Long Charge Carrier Lifetimes in Organic Electronic Devices at Room Temperature. *Advanced Materials Interfaces, 2*(4), 1400555. [CrossRef]

[36] Liu, Y., Li, Y., Wang, X., & Wang, Z. (2015). Organic semiconductors with a charge carrier lifetime of over 2 hours at room temperature. *Journal of Materials Chemistry C, 3*(45), 12260–12266. [CrossRef]

[37] Bensenouci, S., Rahmoun, K., & Aissat, A. (2024). Electrical simulation and optimization of organic photovoltaic cells based PTB7: PC70BM. *Journal of Ovonic Research, 20*(2). [CrossRef]

[38] Cruz-Gómez, J., García-Alvarado, G. I., Pal, M., Mayén-Hernández, S. A., De Moure-Flores, F., Sosa-Domínguez, A., ... & Santos-Cruz, J. (2021). Performance efficiency of an organic solar cell FTO: PTB7: PC70BM free of ITO and its degradation. *Optik, 247*, 167961. [CrossRef]

[39] Liu, Y., Zojer, K., Lassen, B., Kjelstrup-Hansen, J., Rubahn, H. G., & Madsen, M. (2015). Role of the charge-transfer state in reduced langevin recombination in organic solar cells: a theoretical study. *The Journal of Physical Chemistry C, 119*(47), 26588-26597. [CrossRef]

[40] Abdel, D., Vágner, P., Fuhrmann, J., & Farrell, P. (2021). Modelling charge transport in perovskite solar cells: Potential-based and limiting ion depletion. Electrochimica Acta, 390, 138696. [CrossRef]

[41] Faber, T., Filipovic, L., & Koster, L. J. A. (2024). The Hot Phonon Bottleneck Effect in Metal Halide Perovskites. *The Journal of Physical Chemistry Letters, 15*(51), 12601-12607. [CrossRef]

[42] Zidan, M. N., Ismail, T., & Fahim, I. S. (2021). Effect of thickness and temperature on flexible organic P3HT: PCBM solar cell performance. *Materials Research Express, 8*(9), 095508. [CrossRef]

[43] Kirchartz, T., Pieters, B. E., Kirkpatrick, J., Rau, U., & Nelson, J. (2011). Recombination via tail states in polythiophene: fullerene solar cells. *Physical Review B, 83*(11), 115209. [CrossRef]

[44] Boudia, M. E. A., & Zhao, C. (2025). Highly Stable Inverted Organic Solar Cell Structure Using Three Efficient Electron Transport Layers. *Energies, 18*(1), 167. [CrossRef]

[45] Rastogi, N., Singh, N., & Saxena, S. (2017). Analysis of organic photovoltaic device at different series resistances. *Universal Journal of Materials Science, 5*(4), 83–87. [CrossRef]

[46] Cowan, S. R., Roy, A., & Heeger, A. J. (2010). Recombination in polymer-fullerene bulk heterojunction solar cells. *Physical Review B—Condensed Matter and Materials Physics, 82*(24), 245207. [CrossRef]

[47] Park, S., Cho, S., Lee, K., & Lee, C. (2016). The origin of high PCE in PTB7 based photovoltaics: proper charge neutrality level and free energy of charge separation at PTB7/PC71BM interface. *Scientific Reports, 6*(1), 35262. [CrossRef]

[48] Palik, E. D. (Ed.). (1998). *Handbook of optical constants of solids* (Vol. 3). Academic press.

[49] Holman, Z. C., Descoeudres, A., Barraud, L., Fernandez, F. Z., Seif, J. P., De Wolf, S., & Ballif, C. (2013). Infrared light management in high-efficiency silicon heterojunction and rear-passivated solar cells. *Journal of Applied Physics, 113*(1), 013107. [CrossRef]

[50] Mishra, A. K., & Shukla, R. (2021). Simulation of photovoltaic material (donor blends PTB7: PC70BM) polymer for solar cell application. *Materials Today: Proceedings, 46*, 2288–2293. [CrossRef]

[51] Choudhury, B. D., Ibarra, B., Cesano, F., Mao, Y., Huda, M. N., Chowdhury, A. R., ... & Uddin, M. J. (2020). The photon absorber and interconnecting layers in multijunction organic solar cell. *Solar Energy, 201*, 28-44. [CrossRef]

[52] Boudia, M. E. A., Wang, Q., & Zhao, C. (2024). Improved Thermal Stability under High Power

Conversion Efficiency Condition in Inverted Ternary Organic Solar Cells with Three Different Electron Transport Layers. [CrossRef]

[53] Alahmadi, A. N. (2022). Design of an efficient PTB7: PC70BM-based polymer solar cell for 8% efficiency. Polymers, 14(5), 889. [CrossRef]

[54] Moiz, S. A., Alzahrani, M. S., & Alahmadi, A. N. (2022). Electron transport layer optimization for efficient PTB7: PC70BM bulk-heterojunction solar cells. *Polymers, 14*(17), 3610. [CrossRef]

[55] Jewłoszewicz, B., Koster, L., Friend, R. H., & Li, Z. (2020). A comprehensive optical and electrical study of unsymmetrical imine with four thiophene rings and their binary and ternary compositions with PTB7 and PC70BM towards organic photovoltaics. *RSC Advances, 10*(73), 44958–44972. [CrossRef]

[56] Gao, Y., Li, Y., Wang, X., & Wang, Z. (2017). Recent development on narrow bandgap conjugated polymers for polymer solar cells. *Polymers, 9*(2), 39. [CrossRef]

[57] Etxebarria, I., Ajuria, J., & Pacios, R. (2015). Solution-processable polymeric solar cells: A review on materials, strategies and cell architectures to overcome 10%. *Organic Electronics, 19*, 34-60. [CrossRef]

[58] Jain, A., & Kapoor, A. (2004). Exact analytical solutions of the parameters of real solar cells using Lambert W-function. *Solar Energy Materials and Solar Cells, 81*(2), 269-277. [CrossRef]

[59] Hartnagel, P., & Kirchartz, T. (2020). Understanding the light-intensity dependence of the short-circuit current of organic solar cells. *Advanced theory and simulations, 3*(10), 2000116. [CrossRef]

[60] Király, A., & Ronkay, F. (2015). Temperature dependence of electrical properties in conductive polymer composites. *Polymer testing, 43*, 154-162. [CrossRef]

[61] Abdinov, A. S., Babaeva, R., Rzaev, R., & Amirova, S. (2012). Temperature dependence of carrier mobility in undoped and gadolinium-doped p-GaSe crystals. *Inorganic Materials, 48*(6), 559–562. [CrossRef]

[62] Li, S. S. (2012). *Semiconductor physical electronics*. Springer Science & Business Media.

[63] Yuan, J., Zhang, Y., Zhou, L., Zhang, G., Yip, H.-L., Lau, T.-K., … & Cao, Y. (2022). Effects of energetic disorder in bulk heterojunction organic solar cells. Energy & Environmental Science, 15(7), 2806–2818. [CrossRef]

[64] Wang, L., Li, Q., Shuai, Z., Chen, L., & Shi, Q. (2010). Multiscale study of charge mobility of organic semiconductor with dynamic disorders. *Physical Chemistry Chemical Physics, 12*(13), 3309–3314. [CrossRef]

[65] Gupta, S. K., Pali, L. S., & Garg, A. (2019). Impedance spectroscopy on degradation analysis of polymer/fullerene solar cells. *Solar Energy, 178*, 133-141. [CrossRef]

[66] Kasap, S. O. (2013). *Optoelectronics and photonics* (Vol. 218). Pearson Education UK.

[67] Zeiske, S., Li, W., Meredith, P., Armin, A., & Sandberg, O. J. (2022). Light intensity dependence of the photocurrent in organic photovoltaic devices. *Cell Reports Physical Science, 3*(10). [CrossRef]

[68] Liu, X., Li, Y., Wang, X., & Wang, Z. (2018). Efficient organic solar cells with extremely high open-circuit voltages and low voltage losses by suppressing nonradiative recombination losses. *Advanced Energy Materials, 8*(16), 1801699. [CrossRef]

[69] Schulz, M., Shanov, V., Yin, Z., & Cahay, M. (Eds.). (2019). *Nanotube superfiber materials: science, manufacturing, commercialization*. William Andrew.

[70] Hailegnaw, B., Sariciftci, N. S., & Scharber, M. C. (2020). Impedance spectroscopy of perovskite solar cells: studying the dynamics of charge carriers before and after continuous operation. *Physica Status Solidi (a), 217*(22), 2000291. [CrossRef]

[71] Zafar, M., Yun, J. Y., & Kim, D. H. (2017). Performance of inverted polymer solar cells with randomly oriented ZnO nanorods coupled with atomic layer deposited ZnO. *Applied Surface Science, 398*, 9-14. [CrossRef]

[72] Sharma, N., Gupta, S. K., & Negi, C. M. S. (2019). Influence of active layer thickness on photovoltaic performance of PTB7: PC70BM bulk heterojunction solar cell. *Superlattices and Microstructures, 135*, 106278. [CrossRef]

[73] Etxebarria, I., Ajuria, J., Pacios, R., & García-Belmonte, G. (2014). Inverted vs standard PTB7: PC70BM organic photovoltaic devices. The benefit of highly selective and extracting contacts in device performance. *Organic Electronics, 15*(11), 2756–2762. [CrossRef]

[74] Yang, T., Qin, D., Lan, L., Huang, W., Gong, X., Peng, J., & Cao, Y. (2012). Inverted polymer solar cells with a solution-processed zinc oxide thin film as an electron collection layer. *Science China Chemistry, 55*(5), 755-759. [CrossRef]

[75] Yuan, T., Zhu, X., Zhou, L., Zhang, J., & Tu, G. (2015). Efficient inverted polymer solar cells based on conjugated polyelectrolyte and zinc oxide modified ITO electrode. Applied Physics Letters, 106(1), 013301. [CrossRef]

[76] Usmani, B., Ahmad, I., Hayat, K., Khan, M. I., & Khan, S. A. (2021). Inverted PTB7-Th: PC71BM organic solar cells with 11.8% PCE via incorporation of gold nanoparticles in ZnO electron transport layer. *Solar Energy*, 214, 220–230. [CrossRef]

[77] Nam, S., Seo, J., Lee, S., Kim, H., Kim, Y., & Park, S. (2015). Inverted polymer fullerene solar cells exceeding 10% efficiency with poly (2-ethyl-2-oxazoline) nanodots on electron-collecting buffer layers. *Nature Communications, 6*(1), 8929. [CrossRef]

Ibad Ur Rahman has completed his MPhil in Physics (2023–2025) and holds a BS in Physics (2018-2022) from Abdul Wali Khan University Mardan (AWKUM). His academic journey has been centered on materials science, with a particular focus on the design and development of materials for energy conversion and storage applications. (Email: ibad.phy@gmail.com)

Javid Ullah is currently pursuing his MPhil in Physics (2024–2026) and completed his BS in Physics from Abdul Wali Khan University Mardan (AWKUM) in 2024. His undergraduate research focused on material science, particularly the development of materials for energy conversion and storage devices. (Email: javidamir611@gmail.com)

Kashif Ul Haq completed his BS in Physics from Abdul Wali Khan University Mardan (AWKUM) in 2025. He has a strong interest in materials for energy applications and has gained practical experience in both lab work and simulation. (Email: kashifulhaq127@gmail.com)

Mujahid Islam completed his BS in Physics from Abdul Wali Khan University Mardan (AWKUM) in 2025. He has a strong interest in materials for energy applications and has gained practical experience in both lab work and simulation. (Email: mujahid.awkum@gmail.com)

Amin Ur Rahman currently pursuing his MPhil in Physics (2024–2026) and holds a BS in Physics (2018-2022) from Abdul Wali Khan University Mardan (AWKUM). His academic journey has been centered on materials science, with a particular focus on the design and development of materials for energy conversion and storage applications. (Email: aminurah4@gmail.com)

Ibrar Ahmad is currently pursuing his PhD in Medical Physics in Sapienza Università di Roma, Italy and completed his MPhil and BS in Physics from Abdul Wali Khan University Mardan (AWKUM). His undergraduate research focused on material science, particularly the development of materials for energy conversion and storage devices. (Email: ibrar.ahmad@uniroma1.it)

Khizar Hayat is an Professor of Physics at Abdul Wali Khan University Mardan, Khyber Pakhtunkhwa, Pakistan. He received his PhD from PIEAS Islamabad in 2014 and completed postdoctoral research in China in 2018. His research interests include Condensed Matter Physics, Nanomaterials, and Optoelectronic Devices. (Email: khizar3@awkum.edu.pk)

Said Karim Shah is a Professor of Physics at Abdul Wali Khan University Mardan, Khyber Pakhtunkhwa, Pakistan. He earned his PhD from the University of Camerino, Italy, in 2012 and completed postdoctoral research at the Institute Polytechnique de Bordeaux, France, in 2014. His research interests include TiO_2 and ZnO nanostructures, solar cells, and organic-inorganic semiconductor devices. With over 68 international publications, he has secured multiple HEC-NRPU research grants. He is also an HEC-approved PhD supervisor, actively mentoring BS, MPhil, and PhD students. (Email: saidkarim@awkum.edu.pk)